Journal of Catalysis 351 (2017) 119–129

Contents lists available at ScienceDirect

Journal of Catalysis

journal homepage: www.elsevier.com/locate/jcat

Photocatalytic water splitting solar-to-hydrogen energy conversion: Perovskite-type hydride $XBeH_3$ (X = Li or Na) as active photocatalysts

A.H. Reshak *

New Technologies – Research Centre, University of West Bohemia, Univerzitni 8, 306 14 Pilsen, Czech Republic
School of Material Engineering, University Malaysia Perlis, 01007 Kangar, Perlis, Malaysia

ARTICLE INFO

Article history:
Received 28 March 2017
Revised 7 April 2017
Accepted 7 April 2017

Keywords:
Photocatalytic
Perovskite-type hydride $XBeH_3$
DFT

ABSTRACT

A highly enhanced photocatalytic hydrogen production system has been achieved, by substitution of Na by Li and moving from cubic to orthorhombic phase in $XBeH_3$ system. *Ab-initio* calculations from first- to second-principles methods were performed to investigate the suitability of the perovskite-type hydride namely; $NaBeH_3$ and $LiBeH_3$ in cubic phase and $LiBeH_3$ in orthorhombic phase to be used as active photocatalysts. We found significant increases in the fundamental energy band gap when we move from $NaBeH_3$-cubic (0.94 eV) → $LiBeH_3$-cubic (1.34 eV) → $LiBeH_3$-orthorhombic (2.44 eV). The obtained energy band gap's values show good agreement with the previous reported results. Enlarging the fundamental energy band gap from 0.94 → 1.34 → 2.44 eV shows the investigated materials to be promising candidates for light-driven photocatalysts and highly enhanced photocatalytic H_2 production systems. The absorption level of $NaBeH_3$-cubic, $LiBeH_3$-cubic and $LiBeH_3$-orthorhombic exhibited an obvious enhancement in the UV-light region (absorption edge λ = 343.4 nm) → visible light region (λ = 431.9 nm) → UV-light region (λ = 349.2 nm), respectively.

1. Introduction

Energy crises are a global problem and a big challenge at the present time because of the reduction in fossil fuels with high consumption. On the other hand, combustion of fossil fuels is a major source of global pollution [1]. Let us start with global problems of the world; the number one problem is the energy, and is the most important problem that humanity should solve in the near future. The question is, why is energy the number one problem. Well, the evolution of energy consumption can help us to clarify its importance. In recent years, there has been a tremendous increase in energy consumption, and more than 80% of all energy is taken from fossil fuels such as crude oil, coal and natural gas. These fossil fuels are not renewable and one day will vanish, moreover the consumption of fossil fuels causes an increase in the CO_2 concentration in the atmosphere. This is probably the main reason for rising temperature, global worming and climate change. People want to survive and live in a healthy environment; therefore, we should find renewable and eco-friendly sources of energy. How can the energy problem be solved? One of the most efficient solutions is introducing novel photocatalysts, which is the safe and fascinating way that is expected to play an increasingly significant role in facing future energy challenges as a renewable and eco-friendly resource of energy [2].

Photocatalytic water splitting is one of the most promising strategies to achieve clean and renewable solar-to-hydrogen energy conversion [3–9]. The development of visible-light-responsive photocatalysts has been attracting several researchers in recent years [10]. Among the various types of visible-light-responsive photocatalysts, the perovskite-type hydride $XBeH_3$ (X = Na or Li) are introduced, particularly the $LiBeH_3$ in cubic phase because of its well matched optical gap (2.87 eV, λ = 431.9 nm) with the solar spectrum and the sufficient negative conduction band potential for reduction of H^+/H_2 [11–13]. The $XBeH_3$ (X = Na or Li) are promising materials for hydrogen fuel due to their high gravimetric densities; tremendous research work is going on to improve their properties such as reversibility, hydrogen mobility, etc. [14–30]. Vajeeston et al. [20] have used the density functional calculations to investigate the structural phase stability of $MBeH_3$ (M = Li, Na, K, Rb, Cs). Recently, Rehmat et al. [30] have used the density functional calculations to investigate the stability of the perovskite-type hydrides $NaBeH_3$-cubic, $LiBeH_3$-cubic and $LiBeH_3$-orthorhombic; they reported that these hydrides are found to be mechanically stable.

In this work *ab initio* calculations from first- to second-principles methods are performed to investigate the suitability of

* Address: New Technologies – Research Centre, University of West Bohemia, Univerzitni 8, 306 14 Pilsen, Czech Republic. Fax: +420 386 361255.
E-mail address: maalidph@yahoo.co.uk

http://dx.doi.org/10.1016/j.jcat.2017.04.007
0021-9517/

the perovskite-type hydride, namely $NaBeH_3$ in cubic phase and $LiBeH_3$ in orthorhombic phase to be used as active photocatalysts in the UV-light region and $LiBeH_3$ -cubic phase as active photocatalysts in visible light region. In recent years, due to the improvement of computational technologies, it has been proven that the first-principles calculation is a strong and useful tool to predict the crystal structure and properties related to the electron configuration of a material before its synthesis [31–35]. We should emphasize that several researchers have used the first-principles calculation to explore new photocatalysts and found good agreement with the experimental results [36–39].

2. Methodology

First-principles calculations are performed within the framework of density functional theory (DFT) to investigate the suitability of the perovskite-type hydride namely; $NaBeH_3$ and $LiBeH_3$ in cubic phase and $LiBeH_3$ in orthorhombic phase (Fig. 1) to be used as active photocatalysts. The full-potential method (wien2k code [40]) within the generalized gradient approximation (PBE-GGA) [41] is used to optimize the lattice constants [20,24] and the atomic positions [20,24]. The obtained lattice constants and the atomic positions are given in Tables 1–3 in comparison with the available results [20,24]. The recently modified Becke-Johnson potential (mBJ) [42] is used to calculate the ground state properties. Further, the transport properties are performed utilizing the semi-classical Boltzmann theory as incorporated within BoltzTraP code [43] within the limits of Boltzmann theory [44–46] and the constant relaxation time approximation [43].

To ensure that no charge leakage is left out of the atomic sphere cores, the minimum radius of the muffin-tin spheres (R_{MT}) values are set for the $LiBeH_3$- cubic as 2.0, 1.94 and 1.04 a.u. for Li, Be and H atoms, respectively, whereas for the $LiBeH_3$-orthorhombic as 1.7, 1.86 and 1.0 a.u. for Li, Be and H atoms, respectively, and for $NaBeH_3$-cubic as 1.8, 1.74 and 1.1 a.u. for Na, Be and H atoms, respectively. The R_{MT}'s were chosen in such a way that the spheres did not overlap. To achieve the total energy convergence, the basis functions in the interstitial region (IR) were expanded up to $R_{MT} \times K_{max} = 7.0$ and inside the atomic spheres for the wave function. The maximum value of $\boldsymbol{l}$ was taken as $\boldsymbol{l}_{max} = 10$, while the charge density is Fourier expanded up to $G_{max} = 12(a.u.)^{-1}$. Self-consistency is obtained using 1000 $\vec{k}$ points in the irreducible Brillouin zone (IBZ). The self-consistent calculations are converged since the total energy of the system is stable within 0.01 mRy. The electronic properties are calculated using 50,000 $\vec{k}$ points in the IBZ. The total and partial density of states (DOS) are calculated by means of the modified tetrahedron method [47]. The input required for DOS calculating are the energy eigenvalues and eigenfunctions which are the natural outputs of the band structure calculation.

To investigate the thermoelectric properties of the $NaBeH_3$ and $LiBeH_3$ in cubic phase and $LiBeH_3$ in orthorhombic phase, the semi-classical Boltzmann theory as incorporated in BoltzTraP code [43] was used. The transport coefficients based on a rigid band approach to conductivity is given by;

$$\sigma_{\alpha\beta}(\varepsilon) = \frac{1}{N}\sum_{i,k}\sigma_{\alpha\beta}(i,k)\frac{\delta(\varepsilon-\varepsilon_{i,k})}{d\varepsilon} \tag{1}$$

$$\sigma_{\alpha\beta}(i,\vec{k}) = e^2\tau_{i,\vec{k}}\vartheta_\alpha(i,\vec{k})\vartheta_\beta(i,\vec{k}) \tag{2}$$

$$\sigma_{\alpha\beta}(\varepsilon) = \frac{e^2}{N}\sum_{i,k}\tau_{i,\vec{k}}\vartheta_\alpha(i,\vec{k})\vartheta_\beta(i,\vec{k})\delta(\varepsilon-\varepsilon_{i,k}) \tag{3}$$

where e represent charge of electron, τ is the relaxation time, α and β are the tensor indices, N is the number of $\boldsymbol{k}$-points, $\vartheta_\alpha(i,\vec{k})$ and $\vartheta_\beta(i,\vec{k})$ are the group velocities. The transport coefficients can be written as a function of temperature and chemical potential [43,48] as follows;

$$\sigma_{\alpha\beta}(T,\mu) = \frac{1}{\Omega}\int \sigma_{\alpha\beta}(\varepsilon)\left[-\frac{\partial f_0(T,\varepsilon,\mu)}{\partial\varepsilon}\right]d\varepsilon \tag{4}$$

$$S_{\alpha\beta}(T,\mu) = \frac{1}{eT\Omega\sigma_{\alpha\beta}(T,\mu)}\int \sigma_{\alpha\beta}(\varepsilon)(\varepsilon-\mu)\times\left[-\frac{\partial f_0(T,\varepsilon,\mu)}{\partial\varepsilon}\right]d\varepsilon \tag{5}$$

$$\kappa^0_{\alpha\beta}(T,\mu) = \frac{1}{e^2T\Omega}\int \sigma_{\alpha\beta}(\varepsilon)(\varepsilon-\mu)^2\left\{-\frac{\partial f_0(T,\varepsilon,\mu)}{\partial\varepsilon}\right\}d\varepsilon \tag{6}$$

where Ω stands for volume of the unit cell, and f_0 is Fermi–Dirac distribution function. To gain high thermoelectric efficiency, it is important that the material possess high electrical conductivity, large Seebeck coefficient and low thermal conductivity [49].

It is important to highlight that the simulation of the thermoelectric properties is a transition from first- to second-principles methods. The first-principles method used here is all-electron full potential linear augmented plane wave method whereas the second-principles method is BoltzTraP code [43]. The thermoelectric properties were obtained from the ground state within the limits of Boltzmann theory [44–46] and the constant relaxation time approximation as implemented in the BoltzTraP code [43]. In short, BoltzTraP code performs a Fourier expansion of the quantum chemical band energies. This allows us to obtain the electronic group velocity and inverse mass tensor, as the first and second derivatives of the bands with respect to k. Applying the electronic group velocity and inverse mass tensor to the semi-classical Boltzmann equations, the transport tensors can be evaluated.

3. Results and discussion

The photocatalytic activities are directly related to the materials electronic structure [50]. In order to investigate the suitability of the perovskite-type hydride $NaBeH_3$-cubic, $LiBeH_3$-cubic and $LiBeH_3$-orthorhombic to be used as active photocatalysts, the ground state properties are calculated. The calculated electronic band structure explores the value and the nature of the fundamental energy band gaps. Na and Li are alkali metals, have their outermost electron in an s-orbital: this shared electron configuration results in them having very similar characteristic properties. Fig. 2(a) reveals the indirect band gap of the investigated compounds since the valence band maximum (VBM) of $NaBeH_3$-cubic and $LiBeH_3$-cubic is located at X point of the BZ, and the conduction band minimum (CBM) is located at R point, whereas the VBM and the CBM of $LiBeH_3$-orthorhombic are located at U and Γ points resulting in an indirect band gaps. Therefore, the electrons (e) cannot recombine directly with holes (h) thus, it needs the assistance of phonons in order to keep momentum conservation [51–53]. This implies that the investigated compounds may have a long lifetime of photoexcited e and h, which can increase the probabilities for photogenerated e and h to participate in photocatalytic reactions.

We found significant increases in the fundamental energy band gap when we move from $NaBeH_3$-cubic (0.94 eV) → $LiBeH_3$-cubic (1.34 eV) → $LiBeH_3$-orthorhombic (2.44 eV) as shown in Fig. 2(a, b) and Table 4. The obtained fundamental energy band gap's values show good agreement with the previous reported results [20,24,30] as shown in Table 4. Enlarging the fundamental energy band gap from 0.94 → 1.34 → 2.44 eV shows the investigated materials to be promising candidates for light-driven photocatalysts and highly enhanced photocatalytic H_2 production systems. The optical band gap's value of the semiconductor materials could

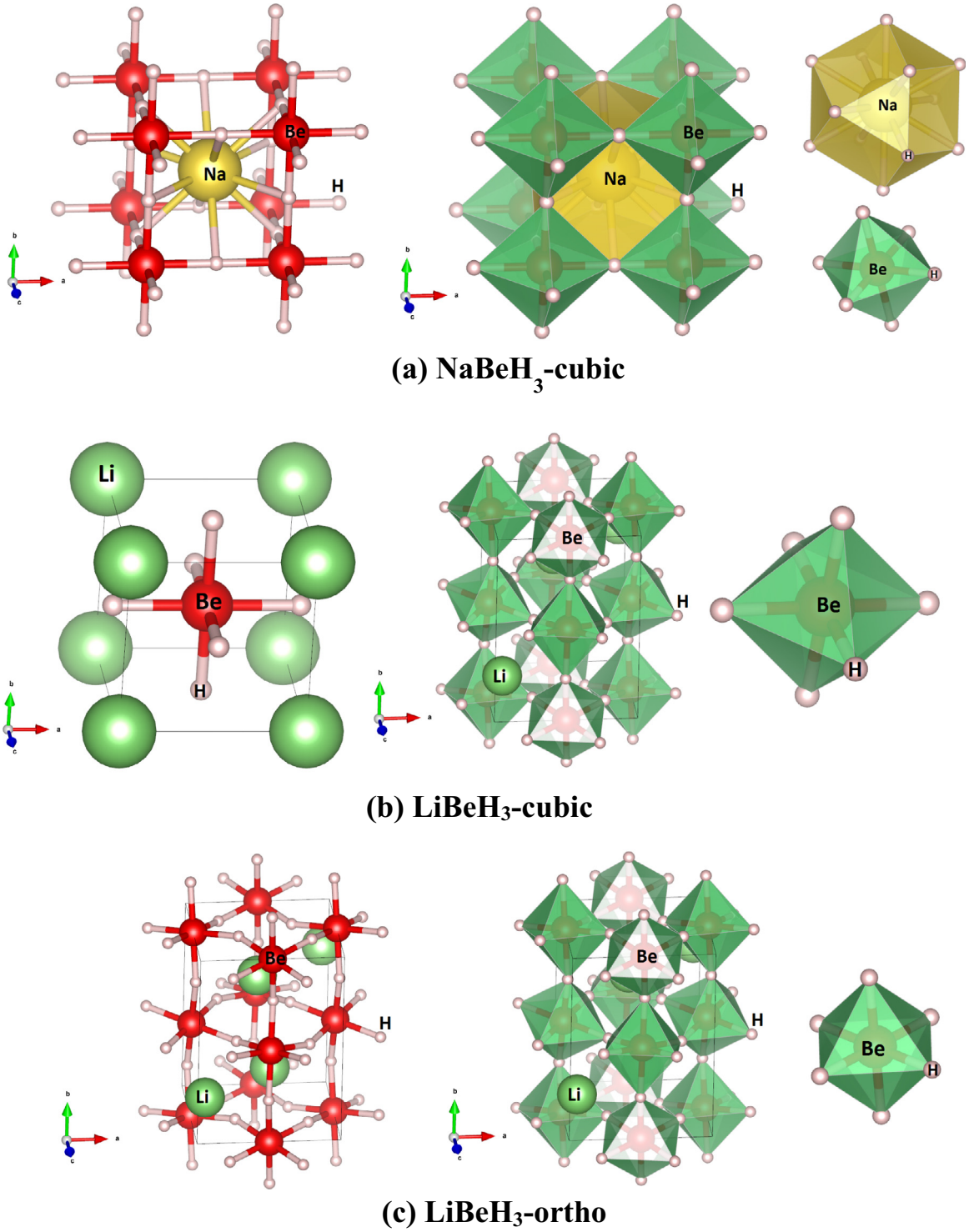

Fig. 1. Crystal structure of the perovskite-type hydride (a) $NaBeH_3$ crystallizes in cubic symmetry with the *Pm-3m* space group (No. 221); (b) $LiBeH_3$ crystallizes in cubic symmetry with the *Pm-3m* space group (No. 221); (c) $LiBeH_3$ crystallizes in orthorhombic symmetry with the *Pnma* space group (No. 62).

be solved as follows; the square of absorption coefficient $I(\omega)$ is linear with energy (E) for direct optical transitions in the absorption edge region, whereas the square root of $I(\omega)$ is linear with E for indirect optical transitions. The calculated electronic band structure confirms the indirect nature of the band gap of the investigated materials; the data plots of the square root of $I(\omega)$ versus E are shown in Fig. 2c. It is clearly shown that the square root of $I(\omega)$ versus E is linear in the absorption edge region. These plots suggest that the absorption edge of the investigated materials is caused by indirect transitions. Following Fig. 2c, we can conclude that the absorption edges of the investigated materials occur at λ = 343.4 nm, λ = 431.9 nm and λ = 349.2 nm, and the optical band

Table 1
Optimized lattice constants and the atomic positions of cubic-$LiBeH_3$ in comparison with the available data [20,24,30].

Cell parameters (Å)		a = b = c	
Exp.		3.190[a], 3.174[b], 3.158[c], 3.122[d]	
This work		3.181	
Atomic positions			
Atom	x[a]	y[a]	z[a]
Li	0.0	0.0	0.0
Be	0.5	0.5	0.5
H	0.0	0.5	0.5

[a] Ref. [24] GGA.
[b] Ref. [24] PBE-GGA.
[c] Ref. [30] WC-GGA.
[d] Ref. [30] LSDA.

Table 2
Optimized lattice constants and the atomic positions of cubic-$NaBeH_3$ in comparison with the available data [24,30].

Cell parameters (Å)		a = b = c	
Exp.		3.318[a], 3.350[b], 3.350[c], 3.281[d]	
This work		3.352	
Atomic positions			
Atom	x[a]	y[a]	z[a]
Na	0.5	0.5	0.5
Be	0.0	0.0	0.0
H	0.0	0.0	0.5

[a] Ref. [24] GGA.
[b] Ref. [24] PBE-GGA.
[c] Ref. [30] WC-GGA.
[d] Ref. [30] LSDA.

gaps are estimated ($\lambda_g = 1239.8/E_{g(optical)}$ [54]) to be 3.61 eV, 2.87 eV and 3.55 eV for $NaBeH_3$-cubic, $LiBeH_3$-cubic and $LiBeH_3$-orthorhombic, respectively.

In the reverse manner, narrowing the energy band gap when we move from $LiBeH_3$-orthorhombic (2.44 eV) → $LiBeH_3$-cubic (1.34 eV) → $NaBeH_3$-cubic (0.94 eV) shows such a small energy band gap material to be a promising candidate for thermoelectric generators. Recently, Niv et al. [55] upended the assumption that the maximal efficiency is considered achievable using a semiconductor within a restricted energy band gap range of 1.1–1.5 eV [56], by demonstrating that the optimal material band gap can be shifted to lower energies by placing selective reflectors around the solar cell. Therefore, following the recent finding of Niv et al. the investigated materials could be used as a solar cell material. This technique opens new possibilities for utilizing materials with a small energy band gap for solar cell applications. Furthermore, Liu et al. [57] have recently reported that narrowing the band gap is beneficial for photoexciton generation and, therefore, the investigated materials could be used as a photocatalyst. The down-shift of the conduction band in the investigated materials ($LiBeH_3$-orthorhombic → $LiBeH_3$-cubic → $NaBeH_3$-cubic) results in narrowing the fundamental energy band gap (Fig. 2a,b), which is believed to be favorable for the generation of photoelectrons with more powerful reducing ability and more strong-oxidating superoxide radicals. Moreover, narrowing the optical band gap allows us to utilize even the weak energy photons efficiently to activate more photoinduced charge carriers participating in the photochemical reactions. The other important factor for a photocatalyst is the optical band gap width, hence, the range of light absorbed (see Fig. 2c). The optical absorption induces the transfer of *e* from the VB → CB, generating the *e–h* pairs which can thence migrate to the surface to participate in oxidation and reduction reactions, respectively [53,58]. Usually the locations of the VBM and the CBM determine the oxidation and reduction capabilities of photogenerated holes and electrons, respectively [53], the reduction potential level of the electron-accepters should be energetically below the CBM whereas the oxidization potential level of the electron-donors should be above the VBM [59].

Back again to the first case (our case) of the enlarging of the optical band gaps, $LiBeH_3$-cubic (2.87 eV) → $LiBeH_3$-orthorhombic (3.55 eV) → $NaBeH_3$-cubic (3.61 eV), the UV -based photocatalyst will perform better per photon than visible light-based photocatalysts due to the higher photon energy, hence, it will possess higher water splitting rates. When photocatalyst absorbs radiation from sunlight, it produces electron-hole pairs. The valence band electrons are excited to conduction band by light illumination, therefore creating the negative electron (e−) and positive hole (h+) pair. This stage is referred as the semiconductor's 'photo-excitation' state. To explain this mechanism in the investigated materials, the carrier concentration as a function of chemical potential ($\mu - E_F$) at three different temperatures is shown in Fig. 3(a–c). It clearly shows the negative electron (n-type conductions) and positive hole (p-type conductions) pair. The positive-hole dissociates the water molecule to form hydrogen gas and hydroxyl radical. The negative-electron reacts with oxygen molecule to form super xide anion. This cycle continues when light is available. To investigate the influence of the temperature on the carrier concentration (electrons and holes), the carrier concentration as a function of temperature at fixed chemical potential ($\mu = E_F$) is shown in Fig. 3 (d–f). Following Fig. 3(d–f) one can see that the carrier concentration in $LiBeH_3$-orthorhombic is almost three times larger than the carrier concentration in the cubic $LiBeH_3$ and $NaBeH_3$. Moreover, it shows that the carrier concentration is constant up to 350 K, then a significant increases occurs with increasing temperature which implies that the 300 K is the optimal temperature. Whereas, in the cubic $LiBeH_3$ and $NaBeH_3$ the carrier concentration decreases with increasing temperature. It has been noted that from the electronic band structure (Fig. 2a) the high k-dispersion bands around Fermi level (E_F) possess low

Table 3
Optimized lattice constants and the atomic positions of orthorhombic-$LiBeH_3$in comparison with the available data [24,30].

Cell parameters (Å)		a		b		c
Exp.		4.517[a], 4.526[b]		6.276[a], 6.293[b]		4.394[a], 4.404[b]
This work		4.523		6.290		4.401
Atomic positions						
Atom	x[a]	x optim.	y[a]	y optim.	z[a]	z optim.
Li	0.04950	0.04830	0.25	0.25	0.98999	0.98976
Be	0.0	0.0	0.0	0.0	0.5	0.5
H1	0.20722	0.20701	0.53693	0.53680	0.20789	0.20771
H2	0.01658	0.01649	0.75	0.75	0.57234	0.57222

[a] Ref. [24].
[b] Ref. [30].

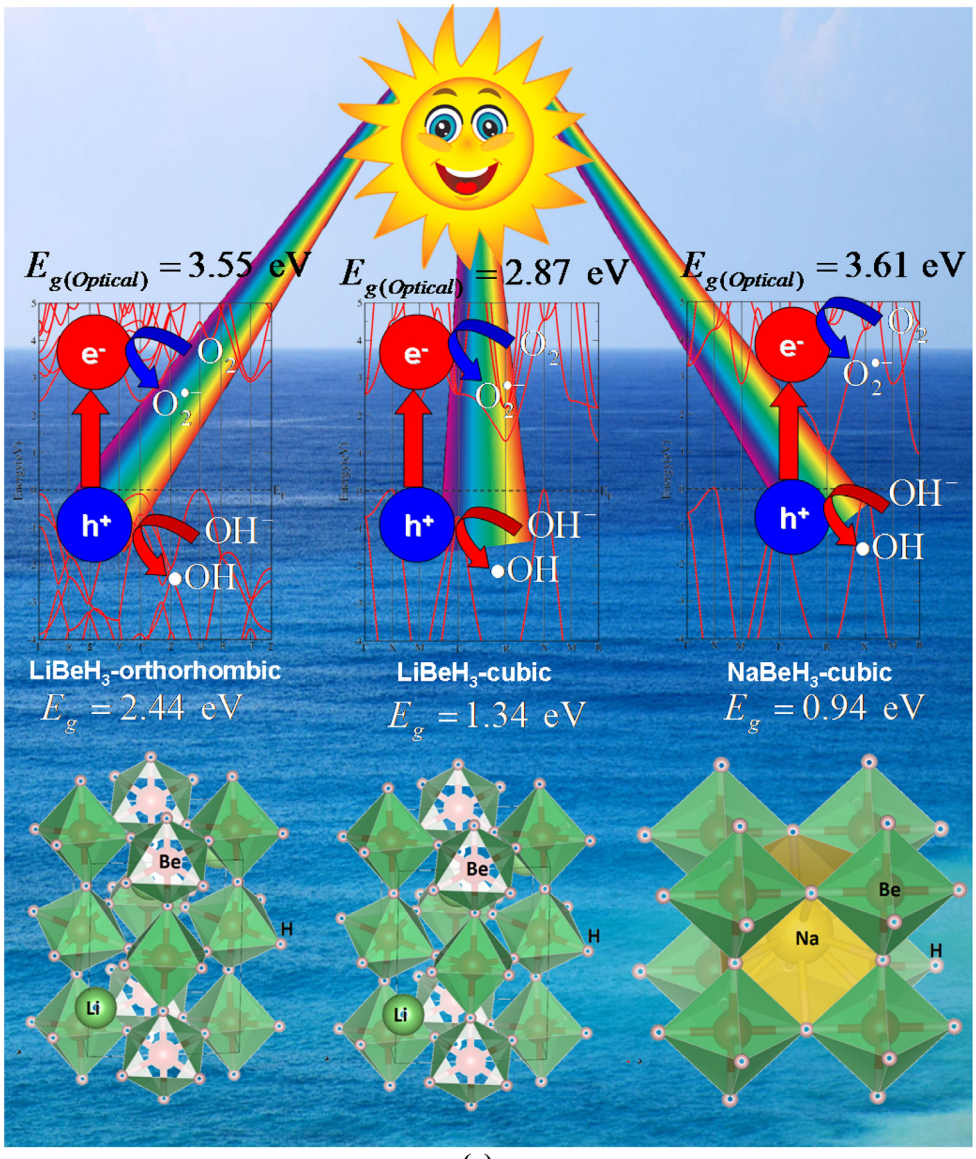

(a)

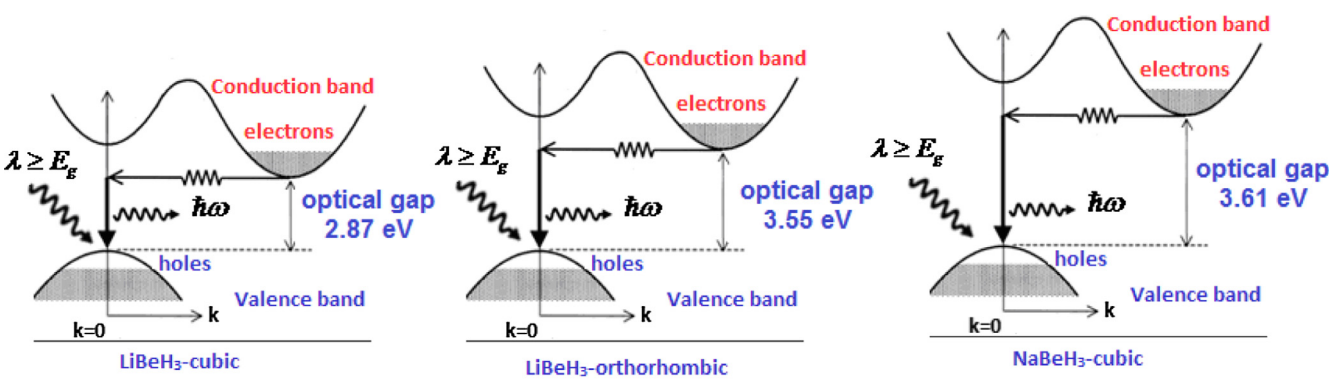

(b)

Fig. 2. (a) Schematic diagrams of charge transfer and photocatalytic mechanism of $NaBeH_3$-cubic, $LiBeH_3$-cubic and $LiBeH_3$-orthorhombic; (b) Schematic of band gap energy level of $NaBeH_3$-cubic, $LiBeH_3$-cubic and $LiBeH_3$-orthorhombic. The up-shift of CB level resulting in enhancing the energy band gap value from 0.94 → 1.34 → 2.44 eV which shows the investigated material to be a promising candidate for light-driven photocatalyst and highly enhanced photocatalytic H_2 production system; (c) The calculated absorption spectrum of $NaBeH_3$-cubic, $LiBeH_3$-cubic and $LiBeH_3$-orthorhombic.

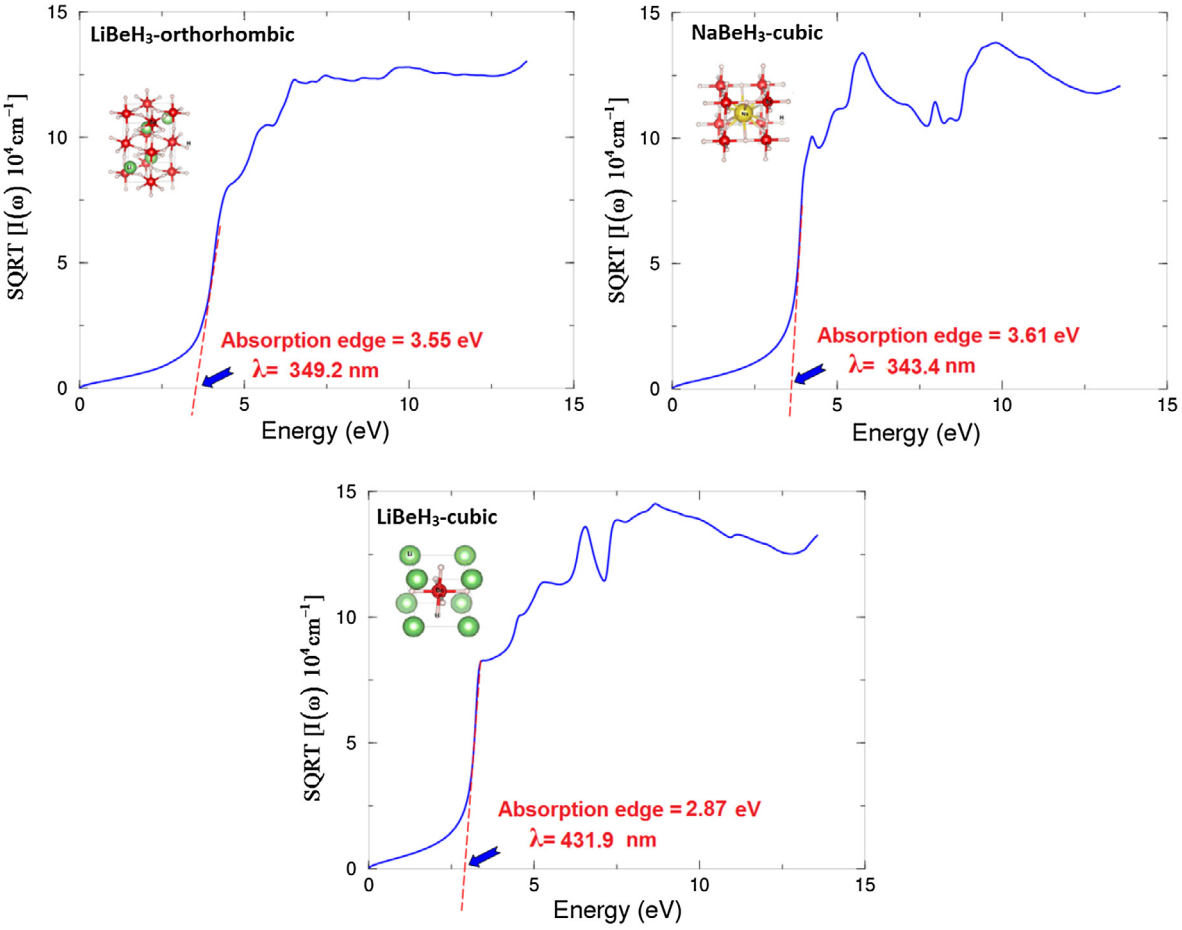

(c)

Fig. 2 (*continued*)

Table 4
Calculated band gaps of orthorhombic-$LiBeH_3$, cubic-$LiBeH_3$, cubic-$NaBeH_3$ compared with the available results obtained from different approximations.

Compound	Band gap (eV)					
	Refs. [20,24]	TB-mBJ Ref. [30]	PBE-GGA Ref. [30]	WC-GGA Ref. [30]	LSDA Ref. [30]	This work
Orthorhombic-$LiBeH_3$	2.26	3.99	2.44	–	–	2.44
Cubic-$LiBeH_3$	1.30	3.24	1.34	1.26	1.24	1.34
Cubic-$NaBeH_3$	1.79	3.16	0.94	0.76	0.85	0.94

effect masses, hence, the high mobility carriers (Table 5) favor enhancing the charge transfer process; the effective mass provides essential information to understand the photocatalytic mechanism. The mobility of the photogenerated carriers significantly influences the photocatalytic efficiency [60,61]; the higher photogenerated carriers' mobility favors enhancing the photocatalytic performance [62]. Moreover, the great effective mass difference ($D = m_e^*/m_h^*$) between electron (e) and hole (h) (see Table 5) can respectively facilitate the migration and separation of e and h, and finally improve the photocatalytic performance. The effective mass of e is bigger than that of the h, resulting in a significant difference in mobility between e and h. The mobility of photoexcited carriers can be indirectly assessed by their effective mass ($\eta_e = e\tau_e/m_e^*$ and $\eta_h = e\tau_h/m_h^*$), here we call the mobility η in order to distinguish between the mobility and chemical potential (μ). The large mobility difference is useful to the separation of e and h, reduction of e and h recombination rate, and improvement of the photocatalytic activity. It is clear from Table 5 that the effective mass of the e and h are small, thus, we can deduce that the photogenerated carriers can fast-transfer along different directions.

Furthermore, to investigate the suitability of the perovskite-type hydride $LiBeH_3$-orthorhombic, $LiBeH_3$-cubic and $NaBeH_3$-cubic to be used as active photocatalysts, the projected density of states along with the angular momentum character of various structures and the electronic charge density distribution are calculated. The projected density of states (Fig. 4) confirm the occurrence of the fundamental energy band gap enlargement when we move from $NaBeH_3$-cubic → $LiBeH_3$-cubic → $LiBeH_3$-orthorhombic. The angular momentum character of various structures (Fig. 4) reveals the type of orbitals which govern the valence and conduction bands, and hence, the fundamental energy band gaps. Also it shows the existence of hybridization between the states, the hybridizations in the VBs broaden the VBs, which can promote the transport capability of the photogenerated holes. The hybridization may lead to form covalent bonding. Covalent bonding is more favorable for the transport of the carriers than ionic bonding [63]. To investigate

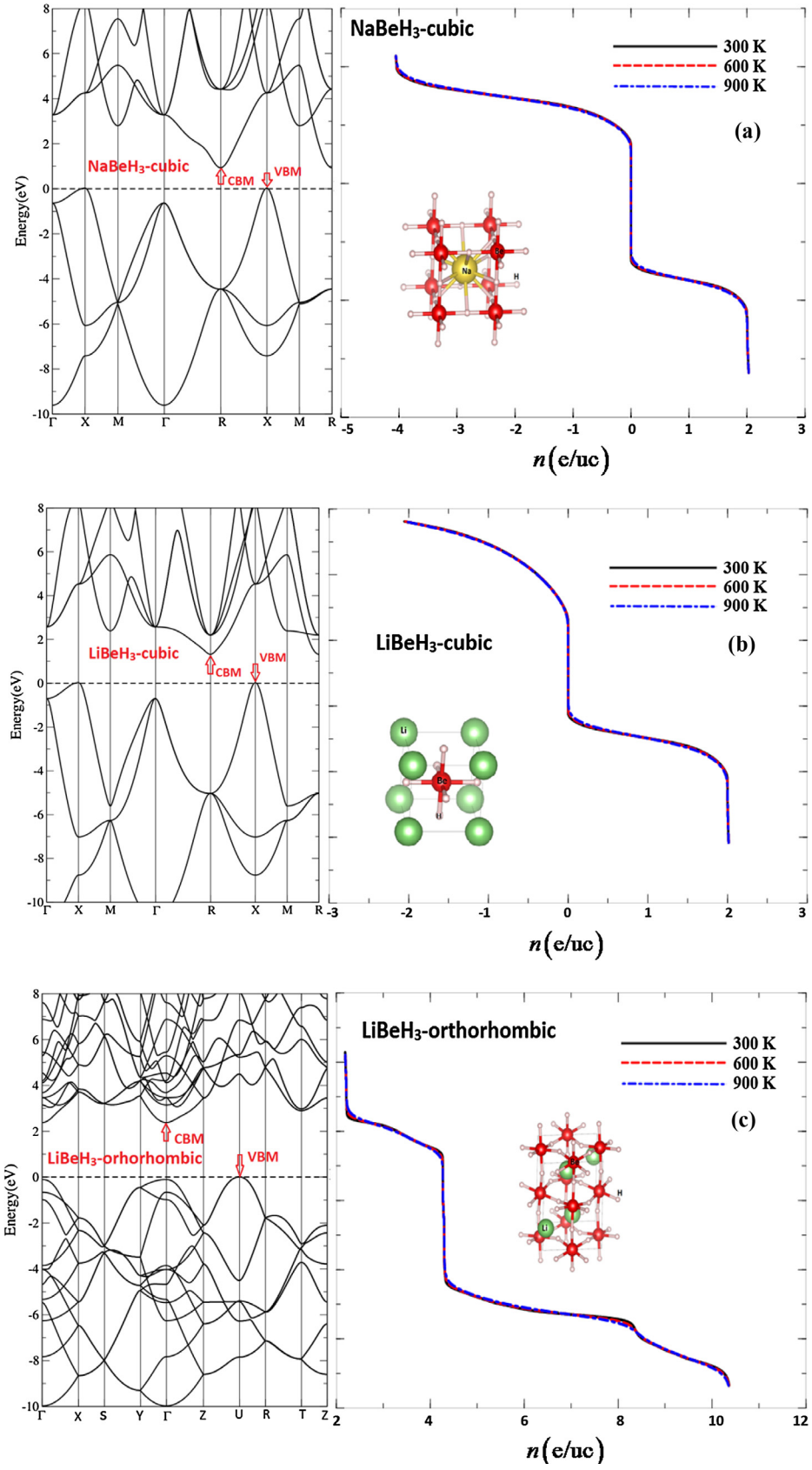

Fig. 3. (a) The carrier concentration of $NaBeH_3$-cubic as function of chemical potential $\mu - E_F$ at room temperature and other two randomly selected temperatures; (b) The carrier concentration of $LiBeH_3$-cubic as function of chemical potential $\mu - E_F$ at room temperature and other two randomly selected temperatures; (c) The carrier concentration of $LiBeH_3$-orthorhombic as function of chemical potential $\mu - E_F$ at room temperature and other two randomly selected temperatures; (d–f) The carrier concentration as a function of temperatures at fixed chemical potential.

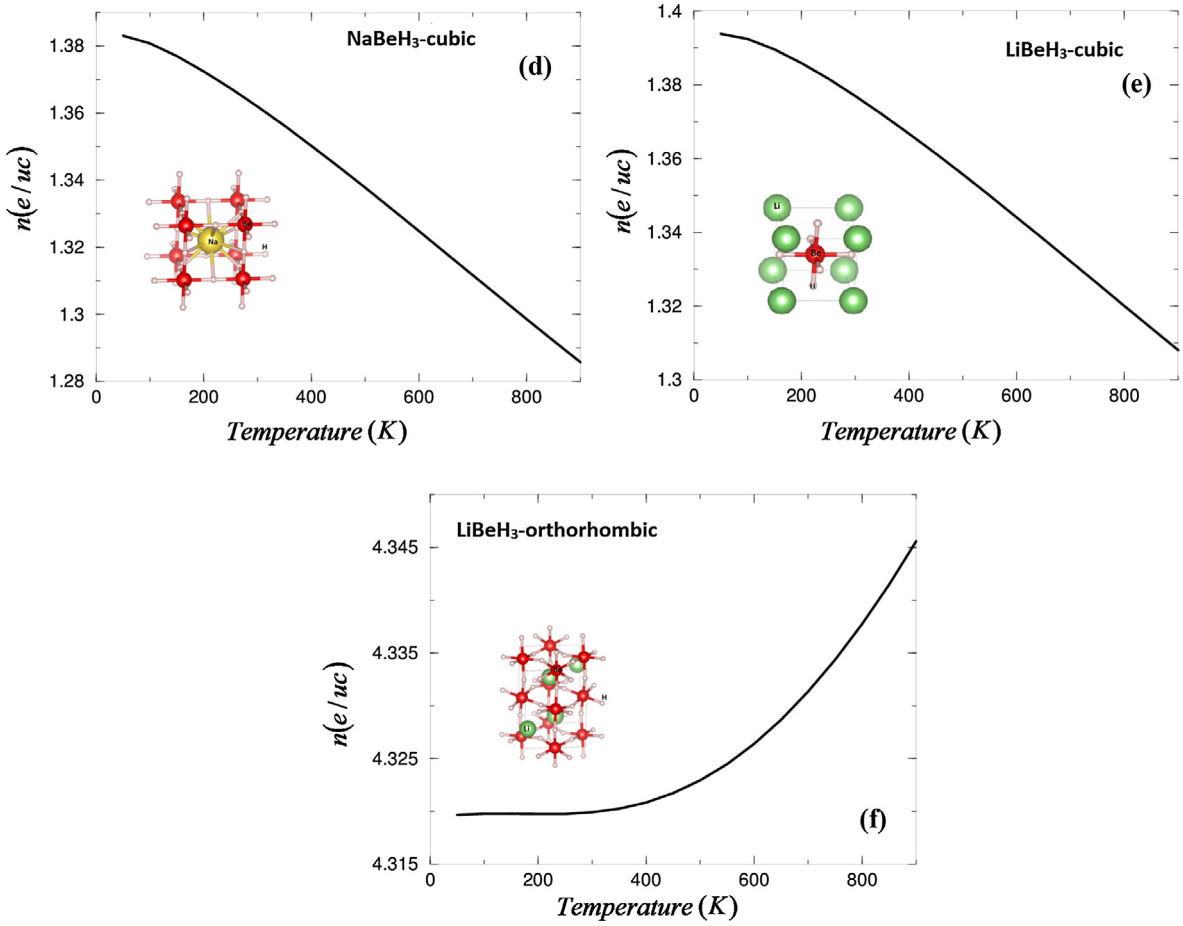

Fig. 3 (*continued*)

Table 5
Calculated effective masses.

Compound	m_e^*/m_o	m_h^*/m_o	$D = m_h^*/m_e^*$	$D = m_e^*/m_h^*$
Orthorhombic-$LiBeH_3$	0.01614	0.01024	0.63444	1.57617
Cubic-$LiBeH_3$	0.02043	0.00431	0.21096	4.74013
Cubic-$NaBeH_3$	0.01286	0.00501	0.38958	2.56686

the carrier concentration, charge transfer and the chemical bonding nature, the electronic charge density distributions are investigated as shown in Fig. 5. The electro-negativity of H, Be, Li and Na are 2.20 > 1.57 > 0.98 > 0.93 according to the Pauling scale, showing that the H atom possesses the highest electro-negativity among them. This implies that efficient charge transfer occurs toward H atoms which is confirmed by Fig. 5, as the H atoms are surrounded by uniform spheres of charge density and the maximum charge accumulates around H atoms as indicated by the blue color (Fig. 5d). The blue color indicates the maximum charge intensity (1.0000) as shown by the thermo-scale (Fig. 5e).

The photocatalytic oxidation of the materials is mainly attributed to the participation of superoxide radicals ($O_2^{\cdot-}$), hydroxyl radicals ($^{\cdot}OH$) and photogenerated holes [64], see Fig. 2a. In order to understand the photocatalytic mechanism of the $NaBeH_3$-cubic, $LiBeH_3$-cubic and $LiBeH_3$-orthorhombic, the reduction and oxidation potentials of the conduction band and the valence band edges at the point of zero charge can be calculated following the expressions given in Ref. [65]:

$$E_{CB} = \chi - E^C - (E_g/2) \quad (7)$$

$$E_{VB} = E_{CB} + E_g \quad (8)$$

where E_{CB} and E_{VB}, respectively, are the potentials of conduction band and the valence band edges, E^C is the free energy corresponding to the hydrogen scale, and the value is ~4.5 eV [65], Eg and χ are the band gap and the electronegativity of semiconductors, respectively. The χ is defined as the geometric mean of the absolute electronegativities of the constituent atoms. The absolute electronegativity of an individual atom is the arithmetic mean of the atomic electron affinity and the first ionization energy [65]. The E_{CB} and E_{VB} values of the $NaBeH_3$-cubic, $LiBeH_3$-cubic and $LiBeH_3$-orthorhombic are shown in Table 6. It can be clearly seen that the CB edge potential becomes more negative with increasing the optical band gap and with substitution of Li by Na, indicating that the $NaBeH_3$ has stronger reduction power for the H_2 production than the $LiBeH_3$. Generally, an appropriate band gap width and suitable CB edge position together attribute to the optimal H_2 production activity under light irradiation. Therefore, a balance between the light absorption capacity and the reduction power in the investigated materials leads to a higher efficiency of light-driven photocatalytic H_2 production.

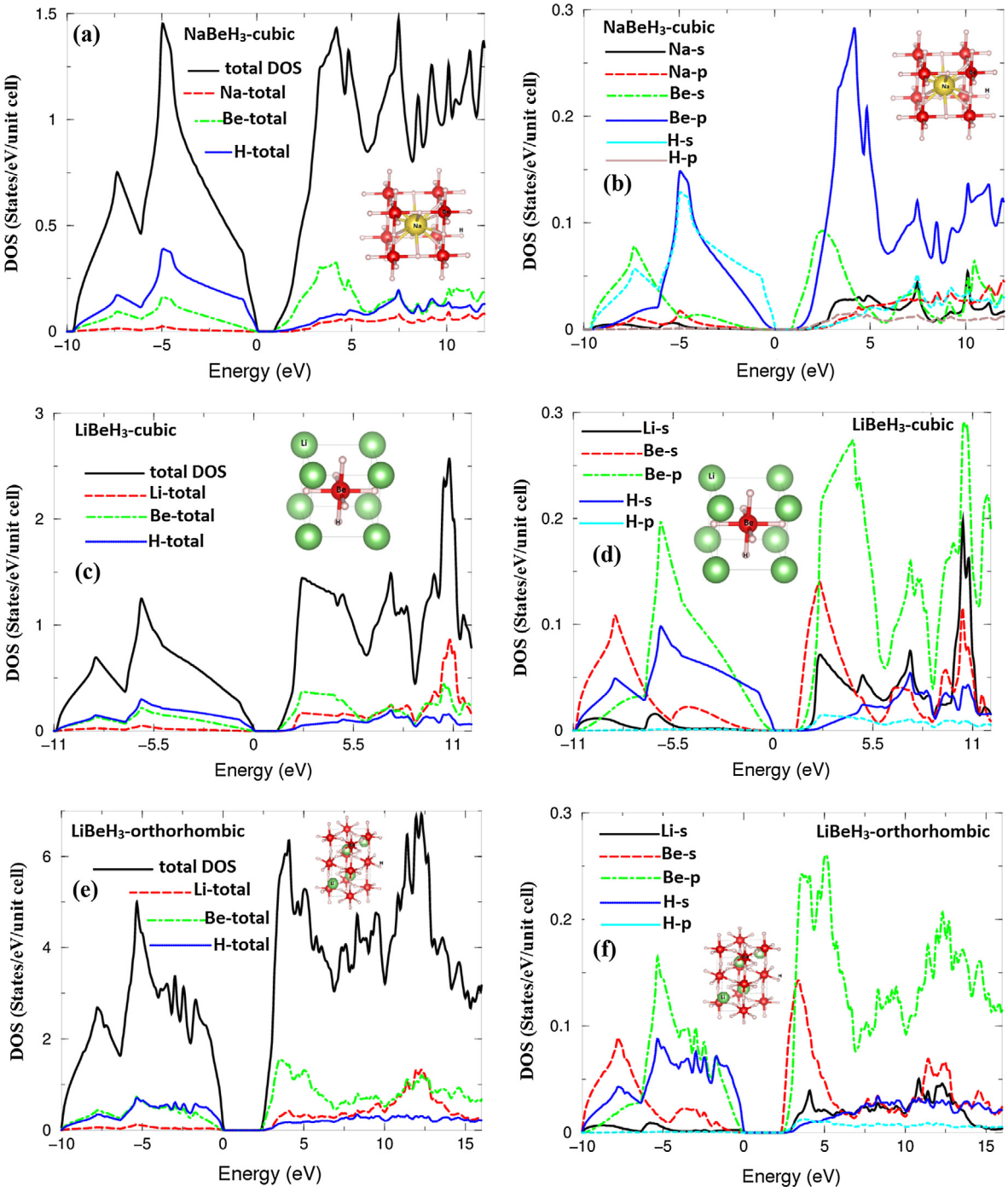

Fig. 4. The projected density of states along with the angular momentum character of various structures.

4. Conclusions

To investigate the suitability of the perovskite-type hydride $LiBeH_3$- orthorhombic, $LiBeH_3$-cubic and $NaBeH_3$-cubic to be used as active photocatalysts, *ab initio* calculations from first- to second-principles methods were performed. Calculations show that a highly enhanced photocatalytic hydrogen production system has been achieved and show significant increases in the fundamental energy band gap when we move from $NaBeH_3$-cubic (0.94 eV) → $LiBeH_3$-cubic (1.34 eV) → $LiBeH_3$-orthorhombic (2.44 eV). Enhancing the fundamental energy band gap value from 0.94 → 1.34 → 2.44 eV shows the investigated material to be a promising candidate for a light-driven photocatalyst and highly enhanced photocatalytic H_2 production system. The calculated absorption spectrum of $NaBeH_3$-cubic, $LiBeH_3$-cubic and $LiBeH_3$-orthorhombic exhibited an obvious enhancement in the UV-light region (absorption edge $\lambda = 343.4$ nm) → visible light region ($\lambda = 431.9$ nm) → UV-light region ($\lambda = 349.2$ nm), respectively. Furthermore, to investigate the suitability of the perovskite-type hydride $LiBeH_3$-orthorhombic, $LiBeH_3$-cubic and $NaBeH_3$-cubic to be used as active photocatalysts, the projected density of states along with the angular momentum character of various structures, the thermoelectric properties and the electronic charge density distribution are calculated. Calculations show that the carrier concentration in $LiBeH_3$-orthorhombic

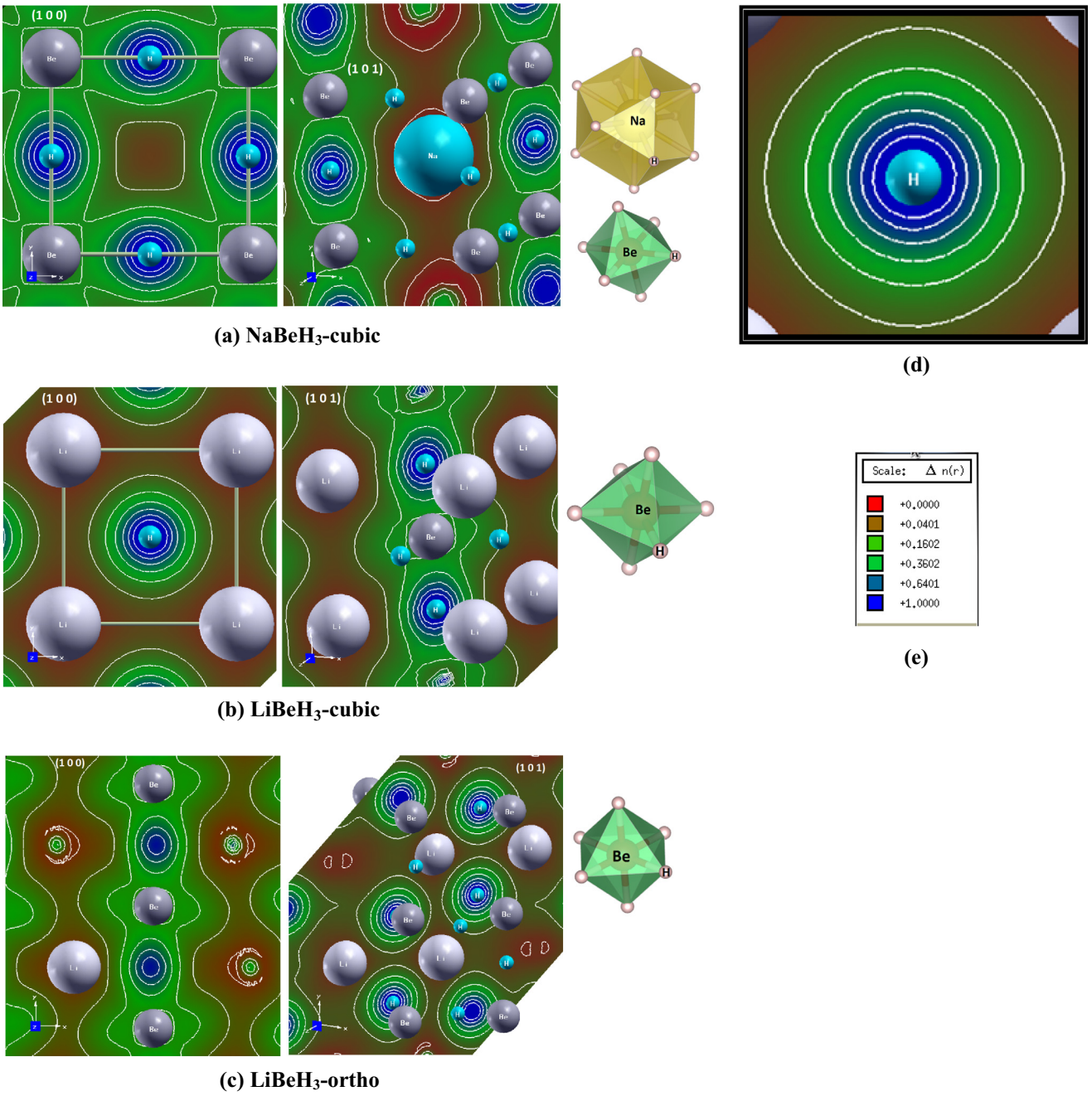

Fig. 5. (a) The charge density distribution of $NaBeH_3$-cubic in (1 0 0) and (1 0 1) crystallographic planes; (b) The charge density distribution of $LiBeH_3$-cubic in (1 0 0) and (1 0 1) crystallographic planes; (c) The charge density distribution of $LiBeH_3$-orthorhombic in (1 0 0) and (1 0 1) crystallographic planes; (d) Shows an efficient charge transfer occurs towards H atoms, as the H atoms are surrounded by uniform spheres of charge density and the maximum charge accumulates around H atoms as indicated by the blue color; (e) thermoscale, the blue color indicates the maximum charge intensity (1.0000).

Table 6
The calculated E_{CB}, E_{VB}, $E_{g(fundamental)}$ and $E_{g(optical)}$ values of the $NaBeH_3$-cubic, $LiBeH_3$-cubic and $LiBeH_3$-orthorhombic.

Compound	E_{CB} (eV)	E_{VB} (eV)	$E_{g(fundamental)}$ (eV)	$E_{g(optical)}$ (eV)
Cubic-$LiBeH_3$	−0.385	2.485	1.37	2.87
Orthorhombic-$LiBeH_3$	−0.725	2.825	2.44	3.55
Cubic-$NaBeH_3$	−0.815	2.795	0.94	3.61

is almost three times larger than the carrier concentration in the cubic $LiBeH_3$ and $NaBeH_3$. The calculations indicate that $NaBeH_3$-cubic, $LiBeH_3$-cubic, $LiBeH_3$-orthorhombic have indirect band gaps, deep position of valence band edge and a strong optical absorption coefficient, implying that $NaBeH_3$-cubic, $LiBeH_3$-cubic, and $LiBeH_3$-orthorhombic have strong oxidation capability and high photocatalytic activity for decomposing organic pollutants under UV and visible light irradiation.

Acknowledgments

The result was developed within the CENTEM project, Reg. No. CZ.1.05/2.1.00/03.0088, cofunded by the ERDF as part of the Ministry of Education, Youth and Sports OP RDI programme and, in the follow-up sustainability stage, supported through CENTEM PLUS (LO1402) by financial means from the Ministry of Education, Youth and Sports under the National Sustainability Programme I. Computational resources were provided by MetaCentrum (LM2010005) and CERIT-SC (CZ.1.05/3.2.00/08.0144) infrastructures.

Appendix A. Supplementary material

The crystallographic cif files of the relaxed structures of $NaBeH_3$-cubic, $LiBeH_3$-cubic, $LiBeH_3$-orthorhombic which was used in this manuscript are provided as supplementary material. Supplementary data associated with this article can be found, in the online version, at http://dx.doi.org/10.1016/j.jcat.2017.04.007.

References

[1] Q. Li, B.D. Guo, J.G. Yu, J. Ran, B.H. Zhang, H.J. Yan, et al., J. Am. Chem. Soc. 133 (2011) 10878–10884.
[2] X.P. Chen, W.F. Shangguan, Front Energy 7 (2013) 111–118.
[3] Zhongli Li, Xiaoping Chen, Wenfeng Shangguan, Yanjie Su, Yijian Liu, Xinwei Dong, Poonam Sharma, Yafei Zhang, Int. J. Hydrogen Energy, http://dx.doi.org/10.1016/j.ijhydene.2016.12.047.
[4] S.U.M. Khan, M. Al-Shahry, W.B. Ingler, Science 297 (2002) 2243–2244.
[5] A. Kudo, Y. Miseki, Chem. Soc. Rev. 38 (253e) (2009) 78.
[6] X.B. Chen, S.H. Shen, L.J. Guo, S.S. Mao, Chem. Rev. 110 (2010) 6503–6570.
[7] H.B. Yi, T.Y. Peng, D.N. Ke, D. Ke, L. Zan, C.H. Yan, Int. J. Hydrogen Energy 33 (2008) 672–678.
[8] C.C. Hu, H. Teng, J. Catal. 272 (2010) 1–8.
[9] K.E. Dekrafft, C. Wang, W.B. Lin, Adv. Mater. 24 (2012) 2014–2018.
[10] N.Z. Bao, L.M. Shen, T. Takata, K. Domen, Chem. Mater. 20 (2008) 110–117.
[11] M. Matsumura, S. Furukawa, Y. Saho, H. Tsubomura, J. Phys. Chem. 89 (1985) 1327–1329.
[12] S.W. Liu, J.G. Yu, M. Jaroniec, J. Am. Chem. Soc. 132 (2010) 11914–11916.
[13] J.R. Ran, J.G. Yu, M. Jaroniec, Green Chem. 13 (2011) 2708–2713.
[14] B. Sakintuna, F. Lamari-Darkrim, M. Hirscher, Int. J. Hydrogen Energy 32 (2007) 1121–1140.
[15] Y. Bouhadda, N. Fenineche, Y. Boudouma, Physica B 406 (2011) 1000–1003.
[16] Y. Li, B. Rao, T. McMullen, P. Jena, P. Khowash, Phys. Rev. B 44 (1991) 6030.
[17] A. Klaveness, O. Swang, EPL (Europhysics Letters) 76 (2006) 285.
[18] M. Fornari, A. Subedi, D.J. Singh, Phys. Rev. B 76 (2007) 214118.
[19] X.-B. Xiao, B.-Y. Tang, S.-Q. Liao, L.-M. Peng, W.-J. Ding, J. Alloy. Compd. 474 (2009) 522–526.
[20] P. Vajeeston, P. Ravindran, H. Fjellvåg, Inorg. Chem. 47 (2008) 508–514.
[21] A. Overhauser, Phys. Rev. B 35 (1987) 411.
[22] M. Seel, A. Kunz, S. Hill, Phys. Rev. B 39 (1989) 7949.
[23] L. Ming, Int. J. Quantum Chem. 68 (1998) 415–419.
[24] S. Xiao-Jiao, H. Zhi, M. Yan-Ming, C. Tian, L. Bing-Bing, Z. Guang-Tian, Chin. Phys. B 17 (2008) 2222.
[25] C.-H. Hu, A. Oganov, Y. Wang, H. Zhou, A. Lyakhov, J. Hafner, Crystal structure prediction of LiBeH (3) using ab initio total-energy calculations and evolutionary simulations, 2008.
[26] P. Vajeeston, P. Ravindran, H. Fjellvåg, J. Alloy. Compd. 446 (2007) 44–47.
[27] E.L.P. y Blancá, Int. J. Hydrogen Energy 41 (2016) 5682–5687.
[28] C.-H. Hu, A.R. Oganov, A.O. Lyakhov, H.-Y. Zhou, J. Hafner, Phys. Rev. B 79 (2009) 134116.
[29] N. Bell, G. Coates, J. Chem. Soc. A: Inorganic Phys., Theor. (1968) 628–631.
[30] Bilal Rehmat, M.A. Rafiq, Y. Javed, Z. Irshad, Nisar Ahmed, S.M. Mirza, Elastic properties of perovskite-type hydrides LiBeH3 and NaBeH3 for hydrogen storage, International journal of hydrogen energy, doi: 10.1016/j.ijhydene.2017.01.109.
[31] M.I. Kolinko, I.V. Kityk, A.S. Krochuk, J. Phys. Chem. Solids 53 (1992) 1315–1320.
[32] G.E. Davydyuk, O.Y. Khyzhun, A.H. Reshak, H. Kamarudin, G.L. Myronchuk, S.P. Danylchuk, A.O. Fedorchuk, L.V. Piskach, M.Yu. Mozolyuk, O.V. Parasyuk, Phys. Chem. Chem. Phys. 15 (2013) 6965.
[33] A.H. Reshak, Phys. Chem. Chem. Phys. 16 (2014) 10558.
[34] A.H. Reshak, Y.M. Kogut, A.O. Fedorchuk, O.V. Zamuruyeva, G.L. Myronchuk, O. V. Parasyuk, H. Kamarudin, S. Auluck, K.L. Plucinskig, J. Bila, Phys. Chem. Chem. Phys. 15 (2013) 18979.
[35] A.H. Reshak, D. Stys, S. Auluck, I.V. Kityk, Phys. Chem. Chem. Phys. 13 (2011) 2945.
[36] H. Huang, Y. He, X. Li, M. Li, C. Zeng, F. Dong, X. Du, T. Zhangd, Y. Zhang, J. Mater. Chem. A 3 (2015) 24547–24556.
[37] H. Huang, Y. He, Z. Lin, L. Kang, Y. Zhang, J. Phys. Chem. C 117 (2013) 22986–22994.
[38] J. Zhang, W. Yu, J. Liu, B. Liud, Appl. Surf. Sci. 358 (2015) 457–462.
[39] X. Li, J. Zhao, J. Yang, Scientific Reports 3 (2013) 1858.
[40] P. Blaha, K. Schwarz, G.K.H. Madsen, D. Kvasnicka, J. Luitz, WIEN2k, An augmented plane wave plus local orbitals program for calculating crystal properties, Vienna University of Technology, Austria, 2001.
[41] J.P. Perdew, S. Burke, M. Ernzerhof, Phys. Rev. Lett. 77 (1996) 3865.
[42] F. Tran, P. Blaha, Phys. Rev. Lett. 102 (2009) 226401.
[43] G.K.H. Madsen, D.J. Singh, Comput. Phys. Commun. 175 (2006) 67–71.
[44] P.B. Allen, In quantum theory of real materials, J.R. Chelikowsky, S.G. Louie (Eds.), Kluwer, Boston, 1996, pp. 219–250.
[45] J.M. Ziman, Electrons and Phonons, Clarendon, Oxford, 2001.
[46] C.M. Hurd, The hall effect in metals and alloys, Plenum, New York, 1972.
[47] P.E. Blöchl, O. Jepsen, O.K. Andersen, Phys. Rev. B Condens Matter. 15;49 (23) (1994) 16223 .
[48] T.J. Scheidemantel, C. Ambrosch-Draxl, T. Thonhauser, J.V. Badding, J.O. Sofo, Phys. Rev. B., 2003, 68, 125210(6).
[49] G.J. Snyder, E.S. Toberer, Nat. Mater. 7 (2008) 105–114.
[50] P. Zhou, J.H. Wu, W.L. Yu, G.H. Zhao, G.J. Fang, S.W. Cao, Appl. Surf. Sci. 319 (2014) 167–172.
[51] M.C. Xu, Y.K. Gao, E.M. Moreno, M. Kunst, M. Muhler, Y. Wang, H. Idriss, C. Wo, Phys. Rev. Lett. 106 (2011) 138302.
[52] J.F. Zhang, P. Zhou, J.J. Liu, J.G. Yu, Phys. Chem. Chem. Phys. 16 (2014) 20382–20386.
[53] Jinfeng Zhang, Yu Weilai, Jianjun Liu, Baoshun Liu, Appl. Surf. Sci. 358 (2015) 457–462.
[54] J.M. Carlsson, B. Hellsing, H.S. Domingos, P.D. Bristowe, Phys. Rev. B 65 (2002) 205122–205132.
[55] A. Niv, Z.R. Abrams, M. Gharghi, C. Gladden, X. Zhang, Appl. Phys. Lett. 100 (2012) 083901.
[56] W. Shockley, H.J. Queisser, J. Appl. Phys. 32 (1961) 510.
[57] Liu Chengyin, Yihe Zhang, Fan Dong, A.H. Reshak, Liqun Ye, Nicola Pinna, Chao Zeng, Tierui Zhang, Hongwei Huang, Appl. Catal. B: Environ. 203 (2017) 465–474.
[58] J.C. Wu, J.W. Zheng, P. Wu, R. Xu, J. Phys. Chem. C 115 (2011) 5675–5682.
[59] S. Banerjee, J. Gopal, P. Muraleedharan, A.K. Tyagi, B. Raj, Curr. Sci. 90 (2006) 1378–1383.
[60] J.W. Tang, J.H. Ye, Chem. Phys. Lett. 410 (2005) 104–107.
[61] T.L. Bahers, M. Rérat, P. Sautet, J. Phys. Chem. C 118 (2014) 5997–6008.
[62] J. Sato, H. Kobayashi, Y. Inoue, J. Phys. Chem. B 107 (2003) 7970–7975.
[63] Fang Wu, Hong Zhang Song, Jian Feng Jia, Xing Hu, Progress in Nat. Sci.: Mater. Int. 23 (4) (2013) 408–412.
[64] P.J. Zhou, G. Yu, M. Jaroniec, Adv. Mater. 26 (2014) 4920–4935.
[65] Q. Li, H. Meng, P. Zhou, Y.Q. Zheng, J. Wang, J.G. Yu, J.R. Gong, ACS Catal. 3 (2013) 882–889.